# Long-Range Cationic Order Collapse Triggered by S/Cl Mixed-Anion Occupancy Yields Enhanced Thermoelectric Properties in Cu5Sn2S7

Gabin Guelou, Pavan Kumar Ventrapati, Virginia Carnevali, Oleg I. Lebedev, Bernard Raveau, Christophe Couder, Carmelo Prestipino, P. Lemoine, Bernard Malaman, Jean Juraszek, et al.

## To cite this version:

Gabin Guelou, Pavan Kumar Ventrapati, Virginia Carnevali, Oleg I. Lebedev, Bernard Raveau, et al.. Long-Range Cationic Order Collapse Triggered by S/Cl Mixed-Anion Occupancy Yields Enhanced Thermoelectric Properties in Cu5Sn2S7. Chemistry of Materials, 2021, 33 (23), pp.9425-9438. 10.1021/acs.chemmater.1c03434 . hal-03515066

HAL Id: hal-03515066
https://hal.science/hal-03515066v1

Submitted on 20 Jan 2022

# Long-range cationic order collapse triggered by S/Cl mixed-anion occupancy yields enhanced thermoelectric properties in $Cu_5Sn_2S_7$

*Gabin Guélou,[1] Ventrapati Pavan Kumar,[1] Virginia Carnevali,[2] Oleg I. Lebedev,[1] Bernard Raveau,[1] Christophe Couder,[1] Carmelo Prestipino,[3] Pierric Lemoine,[3] Bernard Malaman,[4] Jean Juraszek,[5] Christophe Candolfi,[4] Bertrand Lenoir,[4] Rabih Al Rahal Al Orabi,[2] Marco Fornari,[2,]* Emmanuel Guilmeau[1,]**

[1] Laboratoire CRISMAT, UMR 6508, CNRS, ENSICAEN, 6 Boulevard du Maréchal Juin, 14050 Caen Cedex 04, France

[2] Department of Physics and Science of Advanced Materials Program, Central Michigan University, Mt. Pleasant, MI 48859, USA

[3] Univ Rennes, ISCR – UMR 6226, CNRS, F-35000 Rennes, France

[4] Institut Jean Lamour, UMR 7198 CNRS – Université de Lorraine, 2 allée André Guinier-Campus ARTEM, BP 50840, 54011 Nancy Cedex, France

[5] GPM, CNRS, Univ. Rouen, INSA Rouen, UNIROUEN, 76000 Rouen, France

* emmanuel.guilmeau@ensicaen.fr; marco.fornari@cmich.edu

ABSTRACT

In order to investigate pathways to adjust the charge carrier concentration and optimize the thermoelectric properties, we characterized structural properties, thermal stability and thermoelectric performance of pristine and Cl-doped $Cu_{5+\varepsilon}Sn_{2-\varepsilon}S_7$. We demonstrate that Cl doping in $Cu_5Sn_2S_7$-type monoclinic compounds induces a collapse of the long-range cationic ordering, ultimately leading to a sphalerite-type cubic phase characterized by ordered $[Sn(S,Cl)_4]_x$ clusters. The change in crystal structure symmetry upon Cl doping is analyzed by Rietveld refinements against X-ray powder diffraction data, transmission electron microscopy, Mössbauer and X-ray absorption spectroscopy, and low- and high-temperature transport properties measurements. The thermoelectric properties of the so-obtained cubic sphalerite $Cu_{5+\varepsilon}Sn_{2-\varepsilon}S_{7-y}Cl_y$ ($0 \leq \varepsilon \leq 0.133$, $y = 0.35, 0.70$) are strongly enhanced with respect to the undoped $Cu_5Sn_2S_7$: the power factor improves slightly while both electronic and lattice contributions to the thermal conductivity are reduced. Overall, single-phase Cl-doped $Cu_{5.133}Sn_{1.866}S_{7-y}Cl_y$ ($y = 0.35, 0.70$) compounds exhibit high thermoelectric performance, reaching a maximum $ZT$ of 0.45 at 670 K.

## INTRODUCTION

The past few years have witnessed a resurgence of popularity for ternary and quaternary copper sulfides as potential thermoelectric materials.[1,2] Unlike binary copper sulfides, no evidence for performance degradation triggered by ionic conductivity have been reported in these multicomponent systems.[3–5] In absence of ionic conductivity, the dimensionless thermoelectric figure of merit $ZT = S^2T/\kappa\rho$ (where $T$ is the absolute temperature, $S$ is the Seebeck coefficient or thermopower, $\rho$ is the electrical resistivity and $\kappa$ is the total thermal conductivity) characterizes the efficiency by which these compounds convert thermal into electrical energy or vice versa. Significant attention, in the class of copper sulfides, was initially devoted to the mineral tetrahedrites, which exhibits $ZT$ values over unity around 700 K.[1,6–13] Such a renewed interest for thermoelectric copper sulfides has led to the detailed investigation of many other promising complex sulfides, including bornite $Cu_5FeS_4$,[14,15], stannoidite $Cu_8Fe_3Sn_2S_{12}$,[16] germanite derivatives $Cu_{22}Fe_8Ge_4S_{32}$,[17–19] kesterite $Cu_2ZnSnS_4$,[20,21] $Cu_4Sn_7S_{16}$,[22,23] chalcopyrite $CuFeS_2$[24], colusite $Cu_{26}T_2M_6S_{32}$ ($T$ = V, Nb, Ta, Cr, Mo, W; $M$ = Sn, Ge), [25–33] and mohite $Cu_2SnS_3$.[34–42]

Among the numerous investigations that have been performed to date in copper-based sulfides, the Cu-Sn-S system has provided materials with good thermoelectric performance as well as furthered our understanding of the interplay between structure, chemical bonding and physical properties. Indeed, most reported cases of efficient Cu-Sn-S materials involve the simultaneous presence of various structural types derived from the sphalerite structure with different symmetries, cubic (space group $F\bar{4}3m$), tetragonal (space group $I\bar{4}2m$), and monoclinic (space group $Cc$). [34–40] The many competing phases mainly originate from the heterovalency of the Cu-Sn substitution which leads to ordering phenomena (driven by electrostatic interaction); this is in addition to providing effective strategies for tuning the charge carrier concentration.[42,43] The benefits of having numerous phases, cationic disorder, and/or heterogeneous grain boundaries concur to achieve good electrical performances of the conductive network combined with supressed thermal conductivity. The concept of conductive network exemplified by the Cu-S sphalerite matrix has been used to rationalize the physical properties.[29]

At fixed Cu:Sn ratio, doping has been attempted through partial substitutions of In, Zn, Ni, Mn, Fe and Cu for Sn, [36,40,41,44–48] yielding relatively similar outcomes and the formation of at least two different phases. The best performances reported so far have been achieved for the compositions $Cu_2Sn_{0.8}Co_{0.2}S_3$ and $Cu_2Sn_{0.85}Fe_{0.15}S_3$ with maximum *ZT* values of *ca.* 0.85 at 723 K,[36] and *ca.* 0.75 at 723 K,[40] respectively. Distinct strategies involving nano-structuring have also been successful, reaching a *ZT* value of 0.64 at 670 K for blended $Cu_2Sn_{1-x}Zn_xS_3$ nano-bulk samples.[41,44] Three recent investigations of $Cu_{2+x}Sn_{1-x}S_3$ have shown that both structural ordering-disordering and thermoelectric properties are highly sensitive to small variations of chemical compositions.[45–47] For $x \sim 0.15$, an ordered $Cu_5Sn_2S_7$ monoclinic sphalerite-derivative (space group *C2*) was synthesized;[46] the latter was shown to be a degenerate semiconductor with a high carrier mobility and a low figure of merit *ZT* = 0.10 at 700 K. In order to introduce an additional tuning parameter, Deng *et al.* [45] explored Cl-doped $Cu_{2.1}Sn_{0.9}S_3$ reaching a high *ZT* value, approaching 0.80 at 750 K. Doping with Br in the parent $Cu_{2.1}Sn_{0.9}S_3$ has also led to significant increase in the overall thermoelectric performance with a *ZT* value close to unity at 750 K.[48] These interesting preliminary results raise issues regarding the role of Cl for S substitution: does Cl-doping modify the crystal structure? How are the electrical and thermal transport properties impacted?

The stable form at room temperature of copper chloride, γ-CuCl, exhibits the cubic sphalerite structure;[49] we exploited its close structural relationship with $Cu_{2+x}Sn_{1-x}S_3$ sulfides to successfully substitute S for Cl and investigate the impact of the coexistence of Cu-Cl and Sn-Cl with Cu-S and Sn-S bonds over the cationic disorder. For this purpose, we analysed the effect of Cl substitution in a well-ordered sphalerite derivative $Cu_5Sn_2S_7$, synthesized in the presence of Cu overstoichiometry ($x = 0.15$-$0.20$).[46] Our objective is to investigate pathways to adjust the charge carrier concentration using both Cu:Sn ratio variation and Cl doping on the anionic sub-lattice in order to generate cationic disorder while retaining a single-phase material with a Cu-S conductive network. Herein, we report on the collapse of the initial long-range cationic ordering of the $Cu_5Sn_2S_7$ structure by Cl doping in $Cu_{5+\varepsilon}Sn_{2-\varepsilon}S_7$ for $0 \leq \varepsilon \leq 0.133$, leading to the formation of disordered, cubic sphalerite-type thermoelectrics $Cu_{5+\varepsilon}Sn_{2-\varepsilon}S_{7-y}Cl_y$ ($y = 0.35, 0.70$), with an optimized $ZT$ of 0.45 at 670 K.

## RESULTS AND DISCUSSION

### Synthesis and crystal structure

Recently Pavan Kumar *et al.* described the new phase $Cu_5Sn_2S_7$ that crystallizes in a monoclinic ordered sphalerite-derivative structure (space group *C2*) with unit cell parameters $a = 12.0580(5)$ Å, $b = 5.4063(2)$ Å, $c = 8.5026(2)$ Å, and $\beta = 98.163°$.[46] In the original investigation, the samples were prepared by mechanical alloying followed by in-situ crystallization during Spark Plasma Sintering (SPS). In this work, we chose to use high-temperature reaction in sealed silica tube instead (see experimental section) because of concerns related to the use of CuCl as precursor in the ball mill vessels. Stoichiometric $Cu_5Sn_2S_7$ and Cu-rich composition $Cu_{5.133}Sn_{1.866}S_7$ samples have been synthesized with the aim to tune the magnitude of the carrier concentration prior to Cl-doping. Increasing the Cu:Sn ratio to 11/4 (5.133:1.866) provides hole doping, allowing Cl-doping to start from a more metallic sample. Both samples (i.e. $Cu_5Sn_2S_7$ and $Cu_{5.133}Sn_{1.866}S_7$) crystallize in the monoclinic *C2* symmetry,[46] as shown in **figures 1a, 2** and **S1**. Only traces of impurities were found in the sample $Cu_5Sn_2S_7$ (**Fig. S1**). The unit cell parameters of $Cu_{5.133}Sn_{1.866}S_7$ are $a = 12.0742(2)$ Å, $b = 5.4141(1)$ Å, $c = 8.5172(2)$ Å, and $\beta = 98.148(1)°$ (**Table 1**), slightly larger ($V = 551.2$ Å$^3$)

than the pristine phase (V = 548.7 Å$^3$). The structural model was fixed for stoichiometry by placing the extra Cu on the Sn site (**Table 1**). This monoclinic crystal structure, described in the space group *C*2, can be viewed as a derivative of the sphalerite system through cationic ordering in a network of corner-sharing $CuS_4$ and $SnS_4$ tetrahedra (**Figure 2a**).[46] The particular ordering of the $SnS_4$ tetrahedra, with respect to the $CuS_4$ tetrahedra, leads to the formation of $Sn_2S_7$ dimers, completed by a $[Cu_5S_7]_\infty$ tetrahedral framework that forms the conductive network. It has been suggested that the presence of the $Sn_2S_7$ dimers impacts this conductive network by distorting the nearby $CuS_4$ tetrahedra. The latter thus exhibit Cu-S and Sn-S bonds, related to the $Sn_2S_7$ dimers, longer than expected for a sphalerite network.[46,50] The $(Cu^+)S_4$ and $(Sn^{4+})S_4$ tetrahedra, despite being relatively close in size in a sphalerite-derivative structure,[50] clearly tend to order preferentially because of electrostatic long-range interactions. As a consequence, a large number of different phases can be found in the Cu-Sn-S system, even over a small composition range.[45,46] Moreover, small variations in composition lead to the formation of immiscible secondary Cu-Sn-S phases.[46] Such a feature can make tuning of the transport properties a rather complicated task because of the difficulty of adjusting the carrier concentration in a single-phase solid solution. For this reason, Cl-doping appeared as a potential strategy to (re)adjust the number of holes. This form of co-doping with Cu:Sn ratio variation and Cl/S substitution should also help to increase atomic disorder and thus to lower the lattice thermal conductivity. XRPD data analyses indicate that the Cl-doped samples, $Cu_5Sn_2S_{6.65}Cl_{0.35}$ ($Cu_{5+\varepsilon}Sn_{2-\varepsilon}S_{7-y}Cl_y$ with $\varepsilon = 0$, $y = 0.35$), $Cu_{5.133}Sn_{1.866}S_{6.65}Cl_{0.35}$ ($\varepsilon = 0.133$, $y = 0.35$) and $Cu_{5.133}Sn_{1.866}S_{6.3}Cl_{0.70}$ ($\varepsilon = 0.133$, $y = 0.70$) are highly pure. These samples crystallize in the simple cubic sphalerite-type structure (space group $F\bar{4}3m$) suggesting a fully disordered cationic distribution (**Figure 1b**, **Figures 2b** and **S2**). While this loss of cationic ordering might be detrimental in terms of charge carrier mobility, it does, however, offer some interesting prospects in both anion and cation doping while retaining a single-phase material.

This is particularly interesting considering the immiscible character of the Cu-Sn-S phases around the prototypical composition $Cu_2SnS_3$.[46] In fact, as mentioned in the introduction, good thermoelectric performance was reported in multi-phased samples[34,35] such as using Br in order to form a cubic phase.[48] However, the understanding of the structure-properties relationships requires single-phase samples.

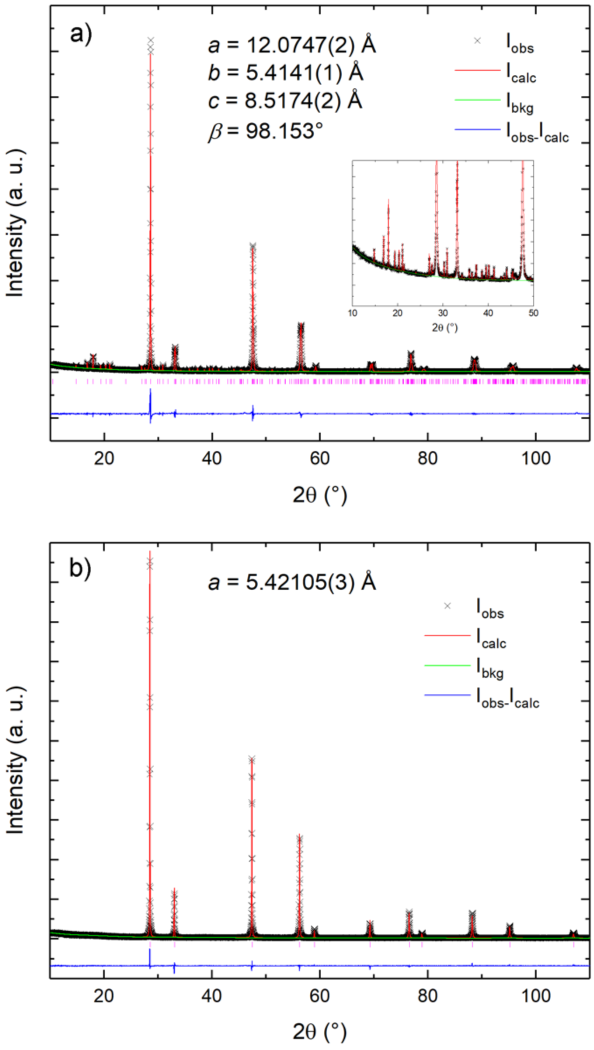

**Figure 1.** Rietveld refinement of XRPD data at room temperature for a) $Cu_{5.133}Sn_{1.866}S_7$ and b) $Cu_{5.133}Sn_{1.866}S_{6.65}Cl_{0.35}$.

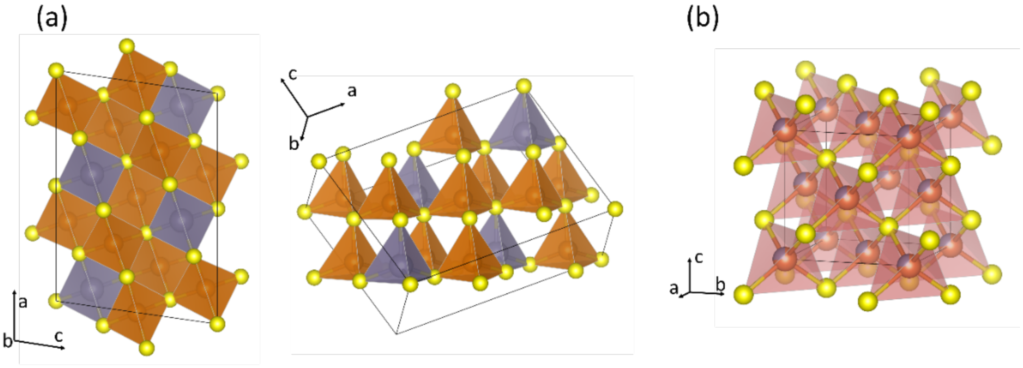

**Figure 2.** Crystal structure representation of (a) $Cu_5Sn_2S_7$ (space group C2) and (b) $Cu_{5.133}Sn_{1.866}S_{6.65}Cl_{0.35}$ (space group $F\bar{4}3m$). Cu and Sn atoms are shown in orange and grey respectively.

**Table 1.** Crystallographic data for $Cu_{5.133}Sn_{1.866}S_7$, $Cu_{5.133}Sn_{1.866}S_{6.65}Cl_{0.35}$ and $Cu_{5.133}Sn_{1.866}S_{6.30}Cl_{0.70}$ obtained by Rietveld refinement of the room temperature X-ray powder diffraction patterns.

| | | | | | |
|---|---|---|---|---|---|
| | | **$Cu_{5.133}Sn_{1.866}S_7$** | | | |
| $a$ (Å) | | 12.0742(2) | Space group | | $C2$ |
| $b$ (Å) | | 5.4141(1) | $R_{wp}$ (%) | | 10.70 |
| $c$ (Å) | | 8.5172(2) | $\chi^2$ | | 1.397 |
| $\beta$ (°) | | 98.148(1) | $\rho$ (g cm$^{-3}$) | | 4.653 |
| Cu(2*b*) | $y$ | 0.780(5) | S(2*a*) | $y$ | 0.013(3) |
| | $B_{iso}$ (Å$^3$) | 2.8(3) | | $B_{iso}$ (Å$^3$) | 1.69 (5) |
| Cu(4*c*) | $x$ | 0.3533(4) | S(4*c*) | $x$ | 0.1475(8) |
| | $y$ | 0.273(3) | | $y$ | 0.020(3) |
| | $z$ | 0.0718(5) | | $z$ | 0.437(2) |
| | $B_{iso}$ (Å$^3$) | 2.0(2) | | $B_{iso}$ (Å$^3$) | 1.69(5) |
| Cu(4*c*) | $x$ | 0.2133(4) | S(4*c*) | $x$ | 0.423(2) |
| | $y$ | 0.283(4) | | $y$ | 0.043(2) |
| | $z$ | 0.6432(6) | | $z$ | 0.292(2) |
| | $B_{iso}$ (Å$^3$) | 2.0(2) | | $B_{iso}$ (Å$^3$) | 1.69(5) |
| Sn/Cu (4*c*) | $x$ | 0.0738(3) | S(4*c*) | $x$ | 0.219(1) |
| | $y$ | 0.289(2) | | $y$ | 0.545(3) |
| | $z$ | 0.2231(4) | | $z$ | 0.145(2) |
| | $B_{iso}$ (Å$^3$) | 1.94(4) | | $B_{iso}$ (Å$^3$) | 1.69(5) |
| | | **$Cu_{5.133}Sn_{1.866}S_{6.65}Cl_{0.35}$*** | | | |
| Space group | | $F\bar{4}3m$ | $R_{wp}$ (%) | | 9.03 |
| $a$ (Å) | | 5.42105(3) | $\chi^2$ | | 0.972 |
| | | | $\rho$ (g cm$^{-3}$) | | 4.606 |
| Cu(4*a*) | SOF | 0.733 | S(4*c*) | SOF | 0.95 |
| | $B_{iso}$ (Å$^3$) | 2.74(2) | | $B_{iso}$ (Å$^3$) | 2.34(4) |
| Sn(4*a*) | SOF | 0.267 | Cl(4*c*) | SOF | 0.05 |
| | $B_{iso}$ (Å$^3$) | 2.74(2) | | $B_{iso}$ (Å$^3$) | 2.34(4) |
| | | **$Cu_{5.133}Sn_{1.866}S_{6.30}Cl_{0.70}$*** | | | |
| Space group | | $F\bar{4}3m$ | $R_{wp}$ (%) | | 10.25 |
| $a$ (Å) | | 5.42424(3) | $\chi^2$ | | 1.714 |
| | | | $\rho$ (g cm$^{-3}$) | | 4.605 |
| Cu(4*a*) | SOF | 0.733 | S(4*c*) | SOF | 0.90 |
| | $B_{iso}$ (Å$^3$) | 3.05(2) | | $B_{iso}$ (Å$^3$) | 2.63(4) |
| Sn(4*a*) | SOF | 0.267 | Cl(4*c*) | SOF | 0.10 |
| | $B_{iso}$ (Å$^3$) | 3.05(2) | | $B_{iso}$ (Å$^3$) | 2.63(4) |

*Cu(4*a*) and Sn(4*a*) on (0, 0, 0) and S(4*a*) and Cl(4*a*) on (¼, ¼, ¼)

## Transmission electron microscopy analysis

Transmission electron microscopy (TEM) analysis was focused on comparing the high purity monoclinic $Cu_{5.133}Sn_{1.866}S_7$ sample with its Cl-doped disordered cubic counterpart, $Cu_{5.133}Sn_{1.866}S_{6.65}Cl_{0.35}$, exhibiting the best thermoelectric performance (see below). For the latter, the electron diffraction (ED) study performed on numerous micro-crystallites collected along the main crystallographic zone axes, confirms the cubic structure and the complete disappearance of the ordering characteristic of the monoclinic structure of $Cu_5Sn_2S_7$. The ED patterns of the Cl-doped samples (**Figure 3**) exhibit a lattice of well-resolved intense spots pointing to the cubic $F\bar{4}3m$ sphalerite structure with the parameter $a$ = 5.42 Å. The associated EDX-STEM elemental mapping confirms the homogeneous distribution of all the elements in the different microcrystals. These observations suggest that Cl for S substitution induces a disordering of the tin and copper cations over the cubic sphalerite sub-lattice, in agreement with the XRPD study. However, beside the intense sphalerite reflections, additional diffuse spots are clearly observed, especially on the [001] and [112] ED patterns (**Figure 3**). Such an observation is compatible with a non-random distribution of the $Sn^{4+}$ and $Cu^{+}$ cations in the cubic sphalerite structure, ultimately forming short-range ordered $Sn_x$ clusters within the copper matrix. This short-range ordering is confirmed by HAADF-STEM images and corresponding Fourier transform (FT) patterns along [001] and [112] zone axes (**Figures 4 a, b**). According to the image simulation based on the cubic structural model with random occupancy of Sn/Cu, all atomic Sn/Cu columns should exhibit equivalent bright contrast (**Figure 4c**). However, the experimental HAADF-STEM images show a clear appearance of higher brightness Sn/Cu columns suggesting Sn-rich or pure Sn (Z = 50) columns as the intensity roughly scales as $Z^n$ with $1 < n < 2$, significantly higher for Sn than Cu (Z = 30). It is worth to notice that pure Sn columns exist along the [010] direction in pristine $Cu_5Sn_2S_7$ (C2).

Their ordering in the (010) plane defines the monoclinic symmetry of the crystal. For $Cu_{5.133}Sn_{1.866}S_{6.65}Cl_{0.35}$, the arrangement of such high-intensity columns maintains a resemblance with the one of $Cu_5Sn_2S_7$ with the presence of some of the characteristic distances and direction between the Sn-rich columns. This suggests that the substitution of Cl for S has a strong effect on long-range periodicity of Cu, but in a less extent on the ordering on the Sn sites, as suggested by the spectroscopic investigations, *vide infra*. The cationic disordering which primarily occurs on the Cu sites is mainly explained by the close structural relationship and "affinity" between CuCl and Cu-S sphalterite-type structures, as stated in the introduction. Based on the obtained experimental ED patterns and HAADF-STEM images, one of the possible models of short-range Sn ordering, with the existence of $[Sn(S/Cl)_4]_4$ clusters randomly distributed, was proposed (**Figure 4c**). The simulated ED pattern obtained from the proposed model shows good correspondence to the experimental one. Interestingly, first-principles formation energy calculations (**Table S1**) indicate that columnar local order, like the one proposed above, is favored with respect to the fully disordered counterpart. Note that theoretical calculations evidence that increasing the Cl content reduces the tendency to form columnar ordering.

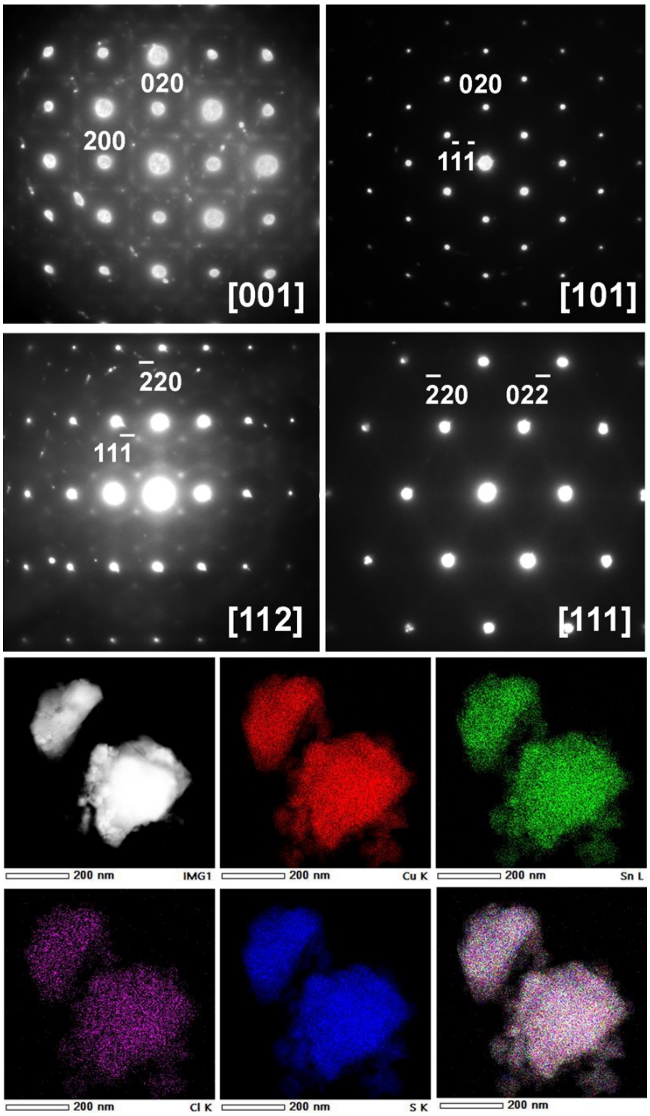

**Figure 3.** ED patterns of $Cu_{5.133}Sn_{1.866}S_{6.65}Cl_{0.35}$ along the main crystallographic zone axes confirming the cubic $F\bar{4}3m$ structure ($a$ = 5.42 Å). Note the presence of additional diffuse spots in [001] and [112] ED patterns resulting from short-range ordering. Low magnification image and simultaneously acquired EDX-STEM elemental mapping of Cu K(red), Sn L(green), Cl K(purple), S K(blue) and overlaid color image. Note the homogeneous distribution of all elements overall the crystal at nanometre scale.

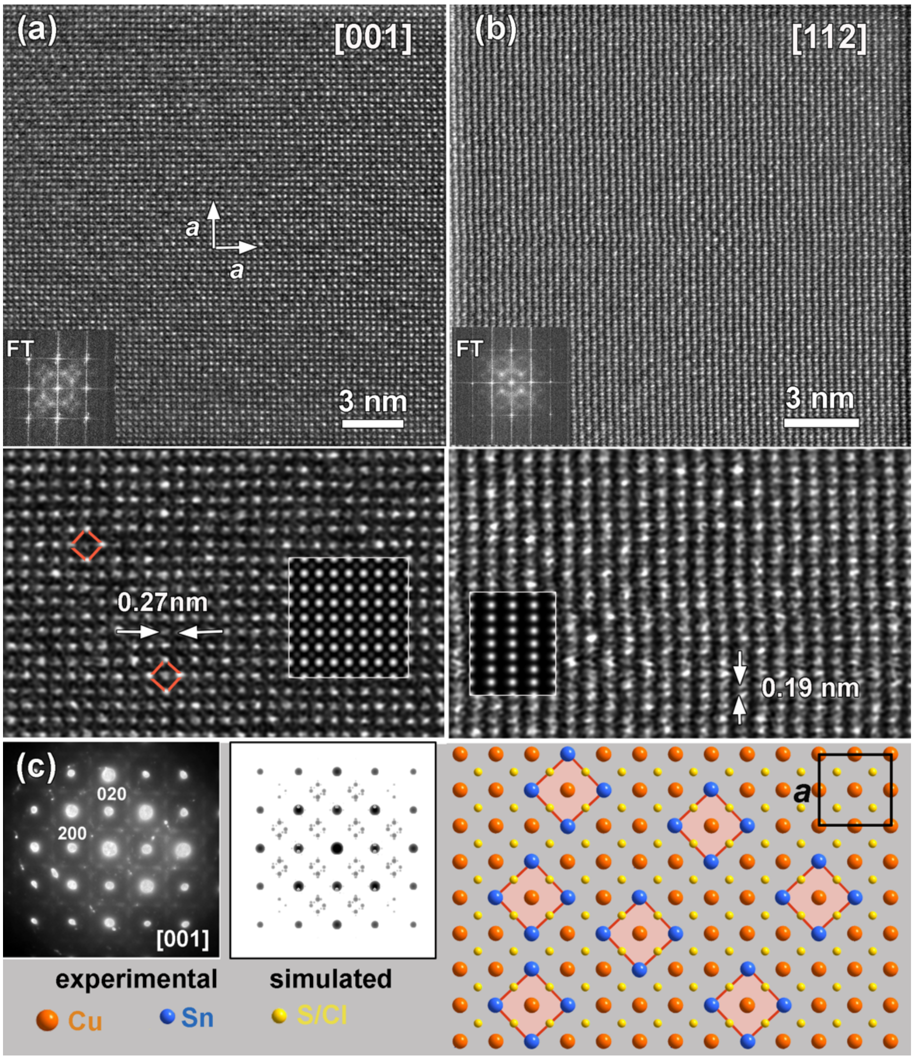

**Figure 4.** High resolution HAADF-STEM images of $Cu_{5.133}Sn_{1.866}S_{6.65}Cl_{0.35}$ along (a) [001] and (b) [112] zone axes and corresponding FT patterns showing clear short-range modulation observed in ED patterns (**Figure 3**). The magnified images and overlaid simulated images are given as inserts. (c) Structural model of short-range structure and corresponding experimental and calculated based on proposal model ED patterns. The short range ordered $[Sn(S/Cl)_4]_4$ clusters are marked by red square frame and pink background. The unit cell parameter of cubic $F\bar{4}3m$ structure ($a$ = 5.42 Å) is indicated by a black box.

The TEM results for $Cu_{5.133}Sn_{1.866}S_7$ sample (**Figure 5**) and collected ED patterns (**Figure 5a**) confirmed the monoclinic $Cu_5Sn_2S_7$ structure (space group $C2$)[46] while EDX-STEM mapping show good chemical homogeneity of the material. The high resolution HAADF-STEM image contrast is in agreement with the structural model and simulated image based on monoclinic *C2* structure (**Figure 5b**). However, the careful analysis of ED patterns revealed the presence of weak streaks along *c*-axis in [010] and [110] ED patterns, suggesting some level of disorder or defects along the *c*-axis. The HAADF-STEM studies revealed significant levels of defects in the form of stacking faults, antiphase boundaries (APB) and chemical inhomogeneity at the atomic level for most of the crystallites. **Figure 6** shows some examples from the most representative defect regions: the monoclinic structure intergrown with defect structures causing stacking faults and APBs (**Figure 6a**) and the highly defective structure along the *c*-axis (**Figure 6b**) indicating a high degree of disorder of alternating Sn-Cu layers. The observed level of disorder and the presence of defects is consistent with the deviation of the Cu:Sn ratio from the nominal $Cu_5Sn_2S_7$ composition and the presence of additional Cu cations on the Sn site.

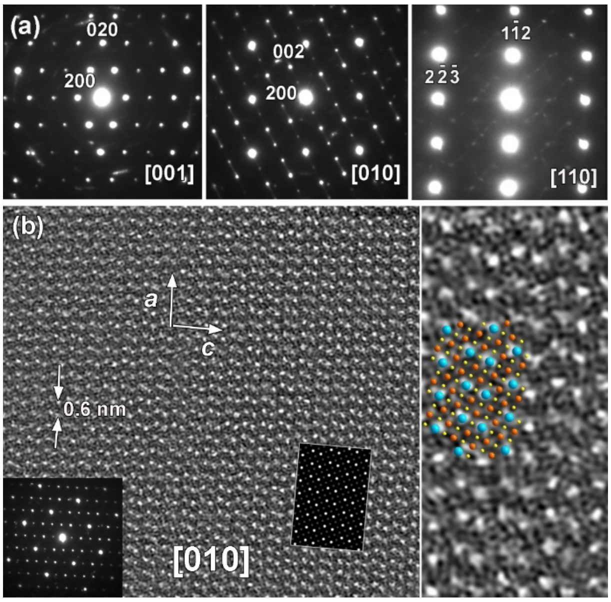

**Figure 5.** (a) ED patterns for $Cu_{5.133}Sn_{1.866}S_7$ along the main crystallographic zone axes confirming monoclinic *C2* structure. Note the presence of streaks and extra spots in [001] and [110] ED patterns. (b) High resolution HAADF-STEM image of good crystalline area of monoclinic structure and corresponding SAED pattern free of any streaks. The simulated image

is given as insert. The magnified image together with overlaid structural model presented in right panel, where Sn-blue, Cu-orange and S-yellow.

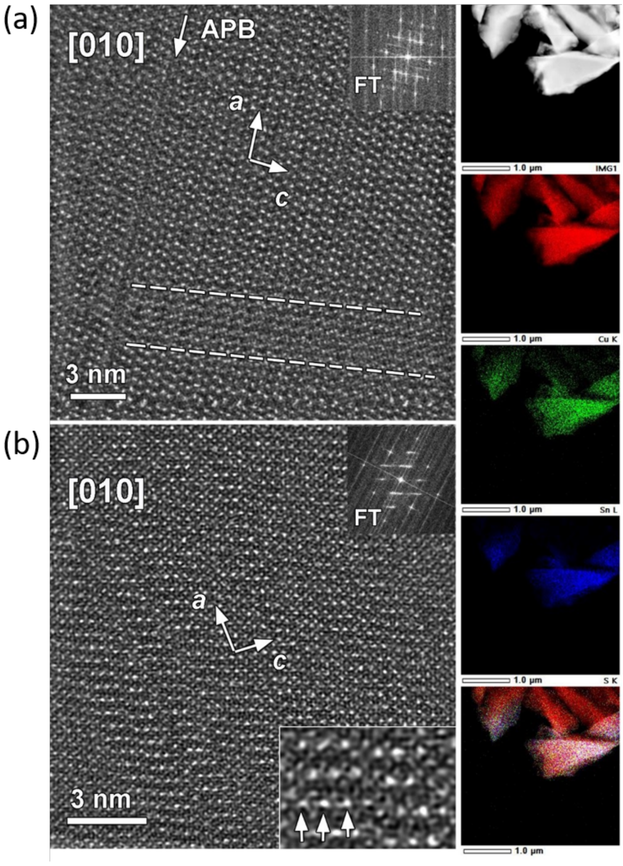

**Figure 6.** High resolution [010] HAADF-STEM images of monoclinic *C2* structure of $Cu_{5.133}Sn_{1.866}S_7$, showing two different types of disordered structures (a) and (b) in the materials (left panel) and corresponding FT patterns given as insert. Note the presence of streaks along c-axis in FT patterns. The low magnification EDX mapping (right panel) evidences a mixture of chemically uniform and non-uniform crystallites within material. The white arrows in magnified high resolution HAADF-STEM image indicate the Sn columns.

**Spectroscopic analyses**

With the aim to go further in the local crystal structure analysis and in the understanding of the anionic distribution around Sn and Cu atoms in the sphalerite-type samples, $^{119}$Sn Mössbauer spectroscopy and X-ray absorption spectroscopy (XAS) analyses were performed.

An isomer shift (IS) value of 1.58 mm $s^{-1}$, was obtained in both $Cu_{5.133}Sn_{1.866}S_7$ and $Cu_{5.133}Sn_{1.866}S_{6.65}Cl_{0.35}$ samples (**Table 2**) from the refinement of the $^{119}Sn$ Mössbauer spectra recorded at 15K (**Figure 7**), indicating that Sn atoms are in their +IV oxidation state[51] and in tetrahedral environment of S atoms.[16,46,52–54] Indeed, the presence of Cl atoms in the first coordination shell of Sn atoms must induce a modification of the valence electron density at the Sn nucleus leading to a decrease of the IS value.[51,55,56] Hence, the identical IS value for the two sphalerite-type samples confirms that a tetrahedral environment of S atoms around Sn atoms is retained regardless of the Cl content. This is in favor of the existence of $[SnS_4]_4$ clusters instead of $[Sn(S,Cl)_4]_x$ clusters in the cubic sphalerite $Cu_{5.133}Sn_{1.866}S_{6.65}Cl_{0.35}$ sample. Consequently, one can expect that Cl atoms are located in the first coordination shell of Cu atoms. This is strongly supported by the existence of the cubic sphalerite γ-CuCl phase.[49]

Both $Cu_{5.133}Sn_{1.866}S_7$ and $Cu_{5.133}Sn_{1.866}S_{6.65}Cl_{0.35}$ samples exhibit higher values of quadrupole splitting ($\Delta E_Q$) and full width at half maximum (FWHM or $\Gamma$) than those refined for the well-ordered monoclinic sphalerite-derivative $Cu_5Sn_2S_7$ phase (**Table 2**). This indicates an increase of the local disorder around Sn atoms induced by both Cu:Sn ratio variation and Cl/S substitution, despite the lower temperature of measurement (reducing the structural disorder through thermal motion). Moreover, these values are higher for $Cu_{5.133}Sn_{1.866}S_{6.65}Cl_{0.35}$ sample compared to $Cu_{5.133}Sn_{1.866}S_7$, especially the $\Delta E_Q$, indicating that Cl for S substitution still increases the degree of structural disorder despite the higher local symmetry of the Sn site: $\bar{4}3m$ in cubic sphalerite structure of $Cu_{5.133}Sn_{1.866}S_{6.65}Cl_{0.35}$ instead of 1 in monoclinic structure of $Cu_{5.133}Sn_{1.866}S_7$. These results are in agreement with electron microscopy analyses.

**Table 2** $^{119}Sn$ hyperfine parameters at 15K of the $Cu_{5.133}Sn_{1.866}S_7$ and $Cu_{5.133}Sn_{1.866}S_{6.65}Cl_{0.35}$ samples: isomer shift (IS), quadrupole splitting ($\Delta E_Q$) and FWHM ($\Gamma$). The $^{119}Sn$ hyperfine parameters at 300K of the $Cu_5Sn_2S_7$ sample are given for comparison (from Pavan Kumar *et al.*)[46]. IS values are given with respect to $BaSnO_3$ at room temperature

| Sample | IS<br>mm s$^{-1}$ (±0.01) | ΔE$_Q$<br>mm s$^{-1}$ (±0.01) | Γ<br>mm s$^{-1}$ (±0.01) | T<br>K |
|---|---|---|---|---|
| $Cu_5Sn_2S_7$ | 1.54 | 0.77 | 0.83 | 300 |
| $Cu_{5.133}Sn_{1.866}S_7$ | 1.58 | 0.80 | 0.88 | 15 |
| $Cu_{5.133}Sn_{1.866}S_{6.65}Cl_{0.35}$ | 1.58 | 0.94 | 0.90 | 15 |

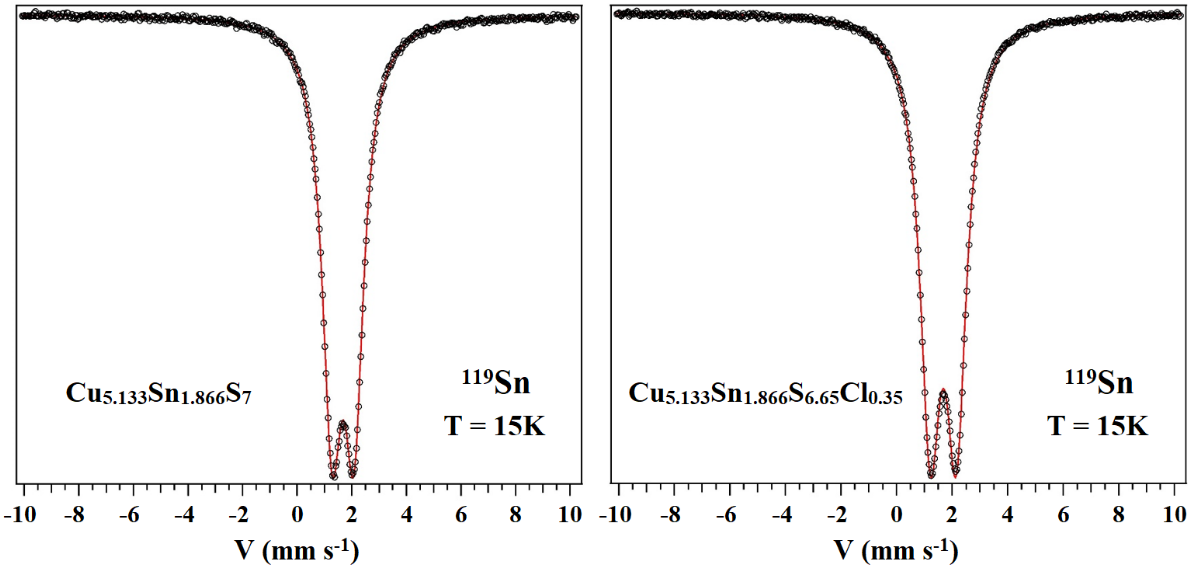

**Figure 7.** $^{119}$Sn Mössbauer spectra recorded at 15K of the monoclinic sphalerite-derivative $Cu_{5.133}Sn_{1.866}S_7$ (space group $C2$) and cubic sphalerite-type $Cu_{5.133}Sn_{1.866}S_{6.65}Cl_{0.35}$ (space group $F\bar{4}3m$) samples. Experimental data and least-squares fits are represented by black crosses and red lines, respectively.

**Figure 8a** shows XANES spectra at the Cu K edge for $Cu_{5.133}Sn_{1.866}S_7$ and $Cu_{5.133}Sn_{1.866}S_{6.65}Cl_{0.35}$ samples with respect to standard compounds Cu metal, $Cu_2S$ ($Cu^+$ in tetrahedral coordination) and $Cu(NH_3)_4^{2+}$ ($Cu^{2+}$ in tetrahedral coordination). The spectral shape for each sample is very similar, confirming a similar local structure (sphalerite framework with partial substitution of Cu by Sn) for all the samples with the position of the edges indicating an oxidation state +1 for Cu. Two small differences can be seen between $Cu_{5.133}Sn_{1.866}S_7$ and $Cu_{5.133}Sn_{1.866}S_{6.65}Cl_{0.35}$, i.e. the latter exhbits a slight red-shift of the edge (red arrow in **Figure 8a**) and the disappearance of a small contribution at around 8977 eV (blue arrow in **Figure 8a**).

Both features could be attributed to the decrease of a small contribution of $Cu^{2+}$. In particular, the peak at 8977 eV is assigned to the copper quadrupolar transition from 1s → 3d level; only possible for $Cu^{2+}$ as $Cu^{+}$ 3d levels are fully occupied. Such assignment is confirmed by the presence of a similar pre-edge peak in the model compound $Cu(NH_3)_4^{2+}$ (inset **Figure 8a**) or in CuS.[57]

The XANES spectra at Sn K-edge contain comparatively fewer features (**Figure S3a**) due to a large core hole lifetime, ~ 6 eV, with the edge position corresponding to an oxidation state +4 of Sn for both samples. Although the difference in core hole lifetime between the Cu and Sn K-edge prevents a direct comparison, it could be noticed that, for Sn edge, the two spectra are practically superimposed while the Cu spectra are more affected suggesting that Cl for S substitution is mainly located in the first coordination of copper. This supports the $^{119}Sn$ Mössbauer spectroscopy observations (**Figure 7**).

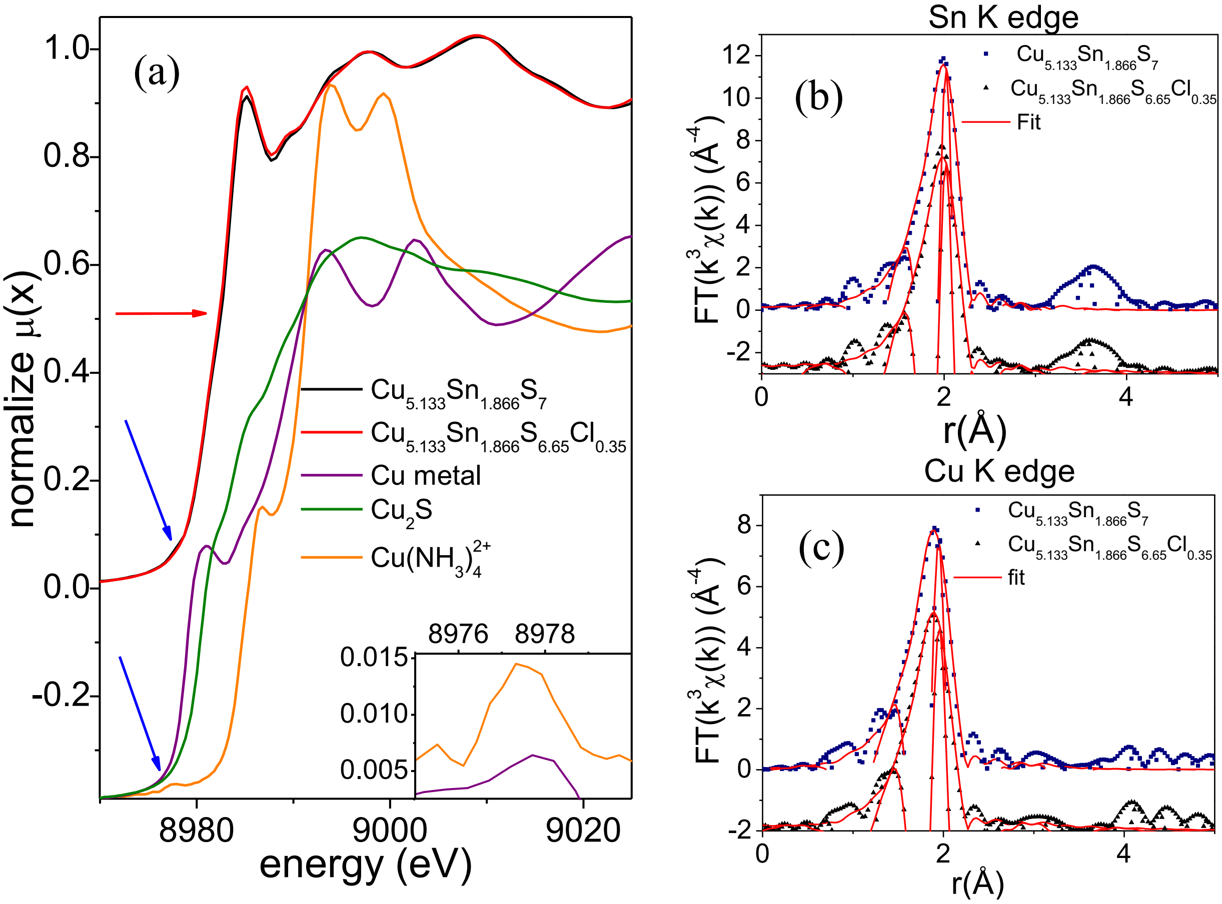

**Figure 8.** XAFS investigation of $Cu_{5.133}Sn_{1.866}S_7$ and $Cu_{5.133}Sn_{1.866}S_{6.65}Cl_{0.35}$ samples. (a) XANES spectra at the Cu K edge with sample and models compounds. Inset: zoom of the pre-edge region with the edge subtracted spectra of $Cu(NH_3)_4^{+2}$ (orange curve) and the difference spectra $Cu_{5.133}Sn_{1.866}S_7$ - $Cu_{5.133}Sn_{1.866}S_{6.65}Cl_{0.35}$ (violet). Fourier transform of EXAFS signals of $Cu_{5.133}Sn_{1.866}S_7$ - $Cu_{5.133}Sn_{1.866}S_{6.65}Cl_{0.35}$ and corresponding fit (red line) at (b) Sn and (c) Cu K edges.

The EXAFS signals for Sn and Cu K edges and results of their analysis are shown in **Figure 8b and 8c,** respectively, while the results of the fit are presented in **Table 3**. The fit model neglects the contribution of Cl; indeed, scattering phase amplitude of S and Cl are very similar and the sample average Cl contribution is limited to ~0.2 (~18.5 % of the cations are coordinated by at least one Cl atom). Both Cu and Sn signals are dominated by a single frequency attributed to the single scattering of sulfur atoms in the first coordination shell. The spectra are very similar and the differences between fit parameters are just above the estimation of standard deviation (**Table 3**). The most noticeable tendency for both edges is the increase of Cu-S and Sn-S bond distances and their associated displacement terms that should be interpreted as an increase of the local structure disorder in agreement with $^{119}$Sn Mössbauer data.

For Sn edge, a small signal around 3.7 Å (not phase corrected) is present for both samples, attributed to the contributions of the second shell, which has not been fitted due to the numerous different components composing the signals. Upon Cl for S substitution, this second shell slightly decreases in intensity but maintains the same shape and phase. It confirms that, apart from a small increase in bond length distribution, the local structure of Sn, up to the second shell (R < 4.5 Å), remains very similar for both samples, supporting the TEM and Mössbauer analyses.

**Table 3.** Summary of the parameters obtained for the combined least square refinements of χ(k) measured at the Sn and Cu K edges for samples $Cu_{5.133}Sn_{1.866}S_7$ and $Cu_{5.133}Sn_{1.866}S_{6.65}Cl_{0.35}$. N, $S_0^2$, R, $\sigma^2$, 3rdcum. and $\Delta E_0$ correspond to degeneracy, passive electron reduction function, distance, mean square relative displacements, third cumulant parameter and shift in the edge energy, respectively.

**Sn K edge $k_{range}$= 3.5-18.3 $Å^{-1}$, $R_{range}$= 1.15 - 2.7Å, fitted in R space with $k^w$=1,2,3**
**Cu K edge $k_{range}$= 3.5-14.5 $Å^{-1}$, $R_{range}$= 1.1 - 3Å, fitted in R space with $k^w$=1,2,3**

| Edge | **Sample** | N | $S_0^2$ | ΔE (eV) | R (Å) | $\sigma^2$ $(Å^2 10^{-3})$ | $3^{rd}$cu $(Å^3 10^{-4})$ | R-fac $k^2$ $10^{-3}$ |
|---|---|---|---|---|---|---|---|---|
| **Cu K** | $Cu_{5.133}Sn_{1.866}S_7$ | 4.0 | 0.80(5) | 1.9(5) | 2.295(5) | 7.9(7) | | 13.3 |
| **Cu K** | $Cu_{5.133}Sn_{1.866}S_{6.65}Cl_{0.35}$ | 4.0 | 0.80(5) | 1.9(5) | 2.300(5) | 8.4(6) | | 10.2 |
| **Sn K** | $Cu_{5.133}Sn_{1.866}S_7$ | 4.0 | 1.15(4) | 5.5(8) | 2.427(7) | 4.9(3) | 1.4(6) | 7.3 |
| **Sn K** | $Cu_{5.133}Sn_{1.866}S_{6.65}Cl_{0.35}$ | 4.0 | 1.15(4) | 5.5(8) | 2.431(7) | 5.7(2) | 2.2(7) | 8.1 |

## Transport properties

The electrical transport properties of the monoclinic $Cu_5Sn_2S_7$ and $Cu_{5.133}Sn_{1.866}S_7$, and the cubic, $Cu_5Sn_2S_{6.65}Cl_{0.35}$, $Cu_{5.133}Sn_{1.866}S_{6.65}Cl_{0.35}$ and $Cu_{5.133}Sn_{1.866}S_{6.3}Cl_{0.70}$ samples measured between 300 and 673 K, are given in **Figure 9**. Pristine monoclinic $Cu_5Sn_2S_7$ exhibits a *p*-type metallic behavior with $\rho$ values ranging between 0.30 mΩ cm and 0.71 mΩ cm at 300 K and 673 K respectively, and *S* values varying between 30 μV $K^{-1}$ and 75 μV $K^{-1}$. These values are fairly consistent with the reported mechanically alloyed $Cu_5Sn_2S_7$,[46] with a slightly lower apparent charge carrier concentration attributed to traces amounts of secondary phases. For the monoclinic (space group *C2*) $Cu_{5.133}Sn_{1.866}S_7$, the formal charge balance can be written as

$$5Cu_{Cu}^{X} + \varepsilon Cu_{Sn}^{'''} + (2-\varepsilon)Sn_{Sn}^{X} + [3\varepsilon + 1]h^{\cdot} + 7S_{S}^{X}$$

which corresponds to a *ca*. 40% increase in the number of holes when compared to $Cu_5Sn_2S_7$ ($\varepsilon = 0.133$). This is reflected by a smaller Seebeck coefficient of *ca*. 21 μV $K^{-1}$ at 300 K, which increases up to *ca*. 59 μV $K^{-1}$ at 670 K. The electrical resistivity has a metallic T-dependence with values ranging from *ca*. 0.25 mΩ cm to *ca*. 0.45 mΩ cm at 300 K and 670 K, respectively. The resulting power factors $S^2/\rho$ for both $Cu_5Sn_2S_7$ and $Cu_{5.133}Sn_{1.866}S_7$ are reasonably high for ternary copper sulfides with a maximum value approaching 0.8 mW $m^{-1}$ $K^{-2}$ at 670 K. This value is close to those observed in colusite, $Cu_{26}V_2Sn_6S_{32}$, or tetrahedrites, $Cu_{12}Sb_4S_{13}$, typically measured around 0.7 – 1.2 mW $m^{-1}$ $K^{-2}$ at 670 K.[9,32] The increase in the Cu:Sn ratio leads to a more metallic behavior allowing more leeway for co-doping with Cl. The transition from a monoclinic to a disordered sphalerite-type cubic structure triggered by Cl doping leads to a significant increase in both $\rho$ and $S$. In fact, Cl-doping in the purer $Cu_{5.133}Sn_{1.866}S_7$ composition shows a more pronounced effect on $\rho$, with an increase by a factor ≈3 and ≈4 at 670 K for $Cu_{5.133}Sn_{1.866}S_{6.65}Cl_{0.35}$ and $Cu_{5.133}Sn_{1.866}S_{6.3}Cl_{0.70}$, respectively. The electrical resistivity of $Cu_5Sn_2S_{6.65}Cl_{0.35}$ is twice that of the pristine phase at 670 K. The impact of Cl is consistent with changes in the hole concentration, supported by the formal charge distribution. Note that Sn was confirmed to be in a +IV oxidation state by $^{119}$Sn Mössbauer spectroscopy, supporting this charge balance description. Note that the upturn in the temperature dependence of the electrical resistivity of $Cu_{5.133}Sn_{1.866}S_{6.30}Cl_{0.70}$ is reminiscent of the dependence observed for the parent colusites, in particular in those containing a significant level of cationic disorder and consequently significant perturbations of the Cu-S conductive network.[31] Such upturn is associated with a change in the transport mechanism and relaxation time, consistent with a strong perturbation of the conductive network, i.e. a large fraction of Cl for S substitution in the present case.

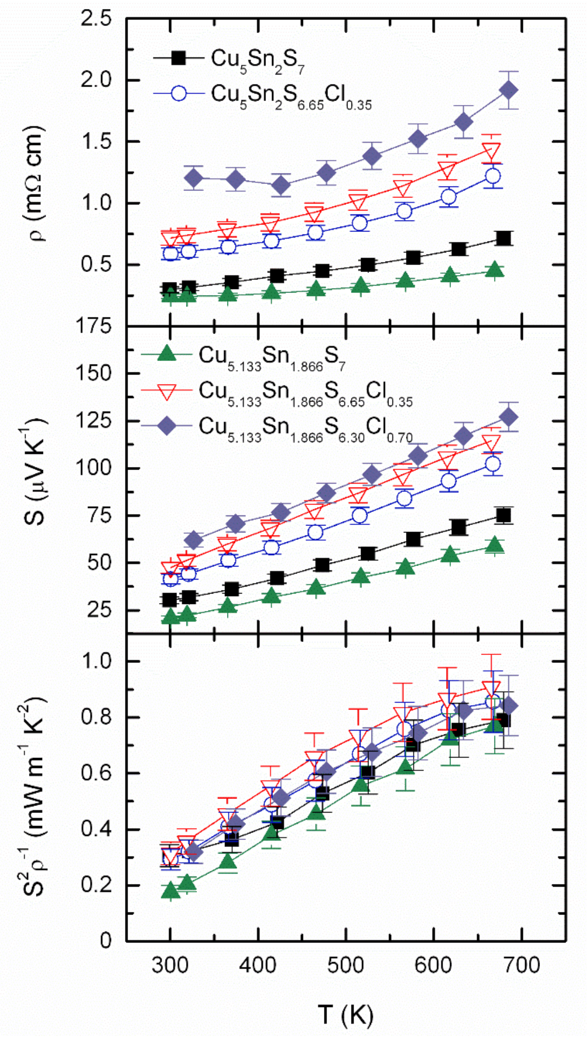

**Figure 9.** Temperature dependence of the electrical resistivity, *ρ*, Seebeck coefficient, *S*, and power factor, $S^2\rho^{-1}$, for monoclinic $Cu_5Sn_2S_7$ and $Cu_{5.133}Sn_{1.866}S_7$, and cubic $Cu_5Sn_2S_{6.65}Cl_{0.35}$, $Cu_{5.133}Sn_{1.866}S_{6.65}Cl_{0.35}$, and $Cu_{5.133}Sn_{1.866}S_{6.3}Cl_{0.70}$.

The hole concentration $p_H$, inferred from measurements of the Hall coefficient $R_H$, decreases with Cl doping in $Cu_{5.133}Sn_{1.866}S_7$ (**Figure S4**) as we would expect from the formal charge balance:

$$5Cu_{Cu}^{X} + \varepsilon Cu_{Sn}^{'''} + (2-\varepsilon)Sn_{Sn}^{X} + [3\varepsilon+1]h^{\cdot} + \left(7 - {}^{n}/_{2}\right)S_{S}^{X} + {}^{n}/_{2}\,Cl_{S}^{'} + {}^{n}/_{2}\,e^{'}$$

with $3\varepsilon + 1 - n/2$ holes per formula unit. With the addition of Cl, the hole concentration is thus decreased by a factor 2 down to 2-3×$10^{21}$ $cm^{-3}$ over the temperature range 50 ≤ T (K) ≤ 300 for $Cu_{5.133}Sn_{1.866}S_{6.65}Cl_{0.35}$.

The low-temperature transport properties (**Figure S5**), measured between 5 and 300 K, confirm the metallic character of both $Cu_{5.133}Sn_{1.866}S_7$ and $Cu_{5.133}Sn_{1.866}S_{6.65}Cl_{0.35}$ down to 5 K. The hole mobility, $\mu_H$, is significantly reduced from *ca.* 9 $cm^2$ $V^{-1}$ $s^{-1}$ for $Cu_{5.133}Sn_{1.866}S_7$ to *ca.* 4 $cm^2$ $V^{-1}$ $s^{-1}$ at 50 K for the cubic $Cu_{5.133}Sn_{1.866}S_{6.65}Cl_{0.35}$ (**Figure S6**) because of the increased cationic disorder. The temperature dependences of $\mu_H$ for $Cu_{5.133}Sn_{1.866}S_7$ and $Cu_{5.133}Sn_{1.866}S_{6.65}Cl_{0.35}$ roughly follow a $T^{-1.5}$ law near room temperature indicative of acoustic phonon scattering. Below room temperature, the weaker $T$ dependence for $Cu_{5.133}Sn_{1.866}S_7$ may be consistent with a $T^{-0.5}$ law related to alloy scattering, a mechanism typically observed in strongly off-stoichiometric compounds.[58–60]Although high-temperature Hall effect measurements would be needed to confirm these trends, this behavior is consistent with previous work suggesting that acoustic phonon scattering prevails above room temperature in these compounds.[35] The high hole mobility of our monoclinic $Cu_{5.133}Sn_{1.866}S_7$ (**Figure S6**), is consistent with that reported for $Cu_{2.1}Sn_{0.9}S_3$.[45] Both phases display a significant decrease in hole mobility upon Cl-doping. This is consistent with the concept of Cu-S conductive network, which suffers from additional charge carrier scattering caused by a disordered cation sublattice. A similar impact was observed in the related colusite family, where significant changes in the transport properties are triggered by structural deformation of the Cu-S conductive network.[31,61]

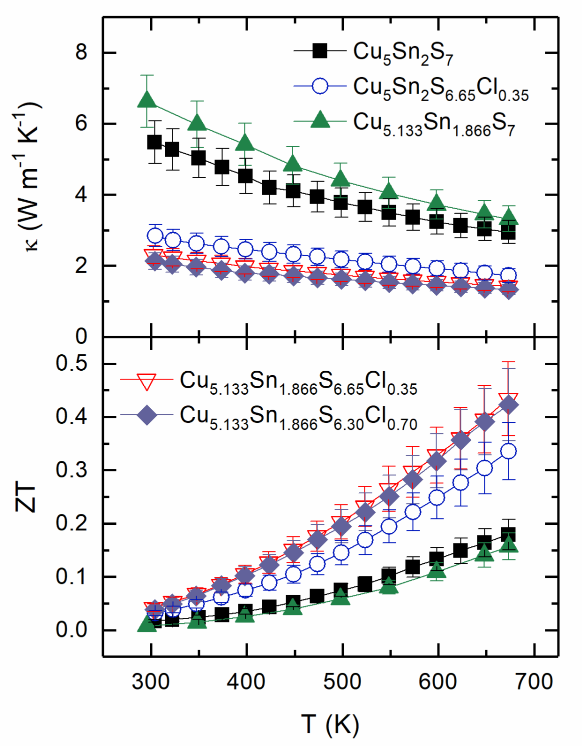

**Figure 10.** Temperature dependence of the total thermal conductivity, *κ*, and dimensionless thermoelectric figure of merit, *ZT*, for $Cu_5Sn_2S_7$, $Cu_{5.133}Sn_{1.866}S_7$, $Cu_5Sn_2S_{6.65}Cl_{0.35}$, $Cu_{5.133}Sn_{1.866}S_{6.65}Cl_{0.35}$, and $Cu_{5.133}Sn_{1.866}S_{6.30}Cl_{0.70}$.

The loss of long-range cationic ordering upon Cl-doping and the transition to a cubic structure are also synergistically beneficial for the thermal transport properties. The total thermal conductivity *κ* for $Cu_{5.133}Sn_{1.866}S_{6.65}Cl_{0.35}$ is significantly reduced compared to the monoclinic $Cu_5Sn_2S_7$ and $Cu_{5.133}Sn_{1.866}S_7$, with values ranging from 2.1 W m$^{-1}$ K$^{-1}$ to 1.3 W m$^{-1}$ K$^{-1}$ at 300 K and 670 K, respectively (**Figure 10**). In order to separate the lattice and electronic contributions from *κ*, the Wiedemann-Franz law was applied by taking into account the temperature dependence of the Lorenz number *L* using a single parabolic band (SPB) model with acoustic phonon scattering (**Figure S7**). As expected from the electrical transport properties, the electronic contribution of the single-phase $Cu_{5.133}Sn_{1.866}S_7$ is slightly higher than that of $Cu_5Sn_2S_7$ with the former exhibiting a very low lattice contribution $\kappa_L$ toward high temperatures. This lowered $\kappa_{\mathrm{lat}}$, despite a similar crystal structure and the absence of secondary phases, may be explained by the rather significant level of cationic disorder observed by HAADF-TEM and related to a slight copper over-stoichiometry. However, the calculated $L$ values for the $Cu_{5.133}Sn_{1.866}S_7$ sample led to doubtful low $\kappa_{\mathrm{lat}}$ values at high temperatures. This inadequacy of the present model to calculate $L$ is due to the multiband nature of the valence band structure of this highly metallic compound that results in lower values than those predicted for a highly-degenerate hole gas using the SPB model. This difficulty in determining the lattice contribution has been highlighted in several thermoelectric materials, such as SnTe, for which the presence of several electronic bands tends to lower the $L$ values despite the strongly degenerate nature of the compound.[62–65] Nevertheless, it seems clear that the nearly three-fold decrease in $\kappa$ observed in Cl-doped samples at 300 K is caused by the simultaneous reduction in both electronic and lattice contributions. The reduction in $\kappa_{\mathrm{lat}}$ is caused by an increased level of cationic disorder, up to a disordered sphalerite-type $Cu_{5.133}Sn_{1.866}S_{7-y}Cl_y$.

## Electronic structure

First-principles density functional theory (DFT) calculations were used to complement the experimental data. Since the virtual crystal approximation has limited validity for our compounds, we studied several models which describe explicitly Cu-Sn local disorder as well as Cl-doping within a supercell approach. Starting by doubling the monoclinic *C*2 cells along the *a* axis (56 atoms), we build six models of the Cu-Sn disorder and doped with Cl (up to three atoms per supercell). A 2 × 2 × 2 cubic supercell (64 atoms), starting from the experimental structure, has been also used to generate 36 models (12 for each Cl concentration). Additionally, a periodic model mimicking the columnar local order observed in ED experiments (cubic, 216 atoms) was also analysed (structural parameters are given in **Table S2**).

The formation energies computed with respect to bulk CuCl, Cu, S, and Sn (**Table S1**) indicate that Cu-Sn as well as Cl disorder minimally affects the formation energies ($\Delta E \leq 25$ meV/atom), and that the cubic ordered structure with $F\bar{4}3m$ symmetry is slightly favored ($\Delta E \sim 40$ meV/atom). As expected, the electronic structure is quite sensitive to disorder and doping, especially in the proximity of the Fermi level ($E_F = 0.0$ eV, the energy reference). The shaded area in **Figure 11** indicates the variation of the DOS with the Cu-Sn disorder. The black curve represents the DOS averaged across several models used to describe cubic $Cu_{5.133}Sn_{1.866}S_{7-y}Cl_y$: $Cu_{23}Sn_9S_{31-m}Cl_m$ with $m = 1, 2$.

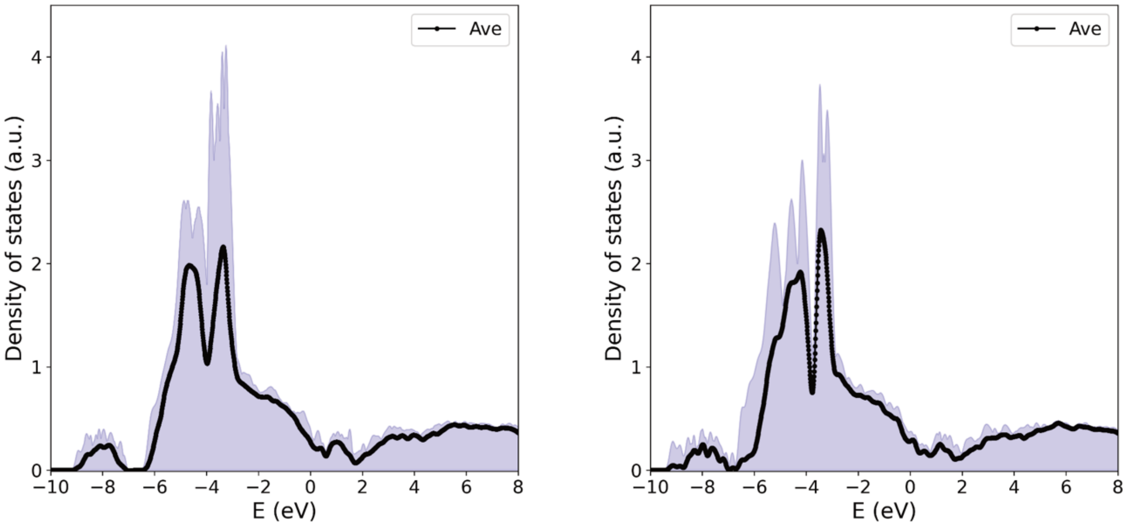

**Figure 11.** Density of states averaged on the several computational cells used to models Cu-Sn disorder. The two panels differ for the Cl concentration (0.35 on the right and 0.70 on the left) and were computed with a 64-atoms cubic cell. In both cases the disorder on the Cu-Sn site lead to electronic states near the Fermi level ($E_F = 0.0$ eV).

Seebeck coefficient and electrical resistivity are also greatly affected by the specific model and hinder our ability to reconcile theory and experiments. In addition, transport calculations within the constant scattering time approximation (CRTA) may fail in the presence of substantial disorder. **Figure S8** illustrates the sensitivity of the theoretical electronic transport coefficients to disorder.

The most interesting theoretical result involves the model used to simulate local ordering effect. Indeed, when considering the structure in **Table 1** that is marginally lower in formation energy (**Table S1**), we obtained slightly better agreement with the experimental transport measurements even within the CRTA (if we optimize the position of the chemical potential). The band structure and the electronic transport coefficient of the ordered 216 atom cell are in **Figure S9 and S10**. The electron localization factor (ELF, **Figure S11**) hints to the formation of Cu-S-Cu linear units that may be responsible for the lower energy.

### Thermal stability

The electrical transport properties measurements for $Cu_{5.133}Sn_{1.866}S_7$ showed some slight discrepancies between values acquired on heating and cooling, suggesting some thermal stability issues. To further explore this possibility, cycling measurements of the electrical transport properties have been carried on $Cu_{5.133}Sn_{1.866}S_7$ and $Cu_{5.133}Sn_{1.866}S_{6.65}Cl_{0.35}$ up to 620 and 670 K, respectively (**Figures 12** and **S12**). As expected, the monoclinic $Cu_{5.133}Sn_{1.866}S_7$ suffers performance losses upon cycling, even at a maximum temperature of 570 K. This is coherent with combined TGA and DSC analysis (**Figure S13**) that displays striking differences between the monoclinic and cubic phases. In particular, while both samples exhibit no weight loss and hence, no sulfur volatilization, the cubic $Cu_{5.133}Sn_{1.866}S_{6.65}Cl_{0.35}$ sample remains completely exempt of any thermal event, all the way up to 800 K. Conversely, monoclinic $Cu_{5.133}Sn_{1.866}S_7$ begins to show signs of instability at around 720 K in the form of a significant exothermic peak in the DSC data. However, the accompanying thermogravimetric analysis does not point towards a large sulphur volatilisation, suggesting that a phase transformation may occur at such high temperature. It is common for complex copper sulphides to undergo a phase transition to a (often cubic) high-temperature phase.[50] This is consistent with the absence of such transition for $Cu_{5.133}Sn_{1.866}S_{6.65}Cl_{0.35}$.

To confirm the stability, repeated measurements of the electrical transport properties of $Cu_{5.133}Sn_{1.866}S_{6.65}Cl_{0.35}$ up to 620 K (5 cycles) and 670 K (5 cycles) have been carried out (**Figure 12**). Unlike its monoclinic counterpart, $Cu_{5.133}Sn_{1.866}S_{6.65}Cl_{0.35}$ clearly retains its electrical performance after the 10 successive cycles. In addition to the improved thermoelectric performance, the enhanced thermal stability of the sphalerite-type $Cu_{5.133}Sn_{1.866}S_{6.65}Cl_{0.35}$ is an extremely promising feature. It is, however, not surprising considering that the high-temperature form of some of the ternary Cu-Sn-S compounds often adopts the cubic sphalerite-type structure through order-disorder phenomena in the cation sublattice.[66]

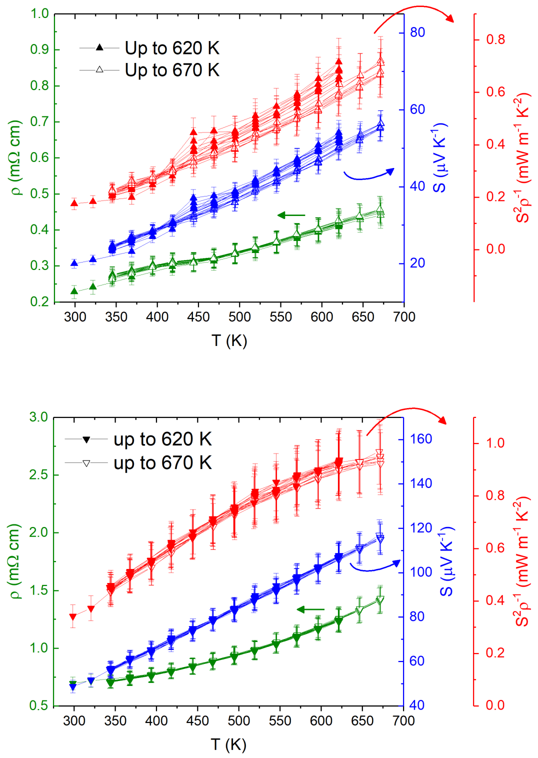

**Figure 12.** Thermoelectric performance of $Cu_{5.133}Sn_{1.866}S_7$ (top) and $Cu_{5.133}Sn_{1.866}S_{6.65}Cl_{0.35}$ (bottom) over the whole stability range, including the electrical resistivity, $\rho$, Seebeck

coefficient, $S$, and power factor, $S^2\rho^{-1}$. Unfortunately, attempts to increase the maximum temperature to 720 K have shown a slight but systematic increase in the electrical resistivity (+2% after 5 cycles).

## CONCLUSION

The ternary Cu-Sn-S system yields a promising series of potential thermoelectric materials, among which the compounds around the prototypical $Cu_2SnS_3$ composition have been reported with excellent performances. Recent progresses, involving high $ZT$ values around 0.7 – 0.8 at 720 K, have been achieved for polymorphic materials.[36,38,40] In this work, we demonstrated that comparable thermoelectric performance can be achieved in a single-phase cubic material with high crystallinity and high relative density through a simple Cl-doping on the sulfur sites. Remarkably, this partial substitution enhances the power factor through an optimized charge carrier adjustment. Concomitantly, the induced increased cationic disordering results in a decrease in the lattice thermal conductivity. These two beneficial effects lead to a maximum $ZT$ of 0.45 achieved at 670 K for $Cu_{5.133}Sn_{1.866}S_{6.65}Cl_{0.35}$. In addition, we demonstrate that this cubic phase displays significantly better thermal stability than its $Cu_5Sn_2S_7$-type counterpart with no sign of deterioration after repeated measurements up to 670 K.[46] All these intriguing results demonstrate that the sphalerite-type conductive network retains its potential for high thermoelectric performance in a disordered cubic phase and removes the need for ordered polymorphic structures. Finally, it is worth pointing out that the loss of long-range ordering triggered by Cl-doping in the $Cu_5Sn_2S_7$-type structure has been observed for a very narrow compositional range in the system $Cu_{2+x}Sn_{1-x}S_3$, $x = 0.15 – 0.20$ and seems to compete with local ordering effects appearing as Sn-rich structures randomly distributed in the matrix. This suggests that the doping of the Cu-Sn-S system by Cl offers a vast playground for further generation of disordered cubic sphalerites in the range $0 \leq x < 0.15$ and enhancement of their thermoelectric properties.

## EXPERIMENTAL SECTION

### *Synthesis*

The polycrystalline samples were synthesized by a two-step solid state reaction in evacuated silica tubes from elemental precursors, Cu (Alfa Aesar, 99 %), Sn (Alfa Aesar, 99.85 %), S (Alfa Aesar, 99.5 %) and CuCl (Alfa Aesar, 99 %). First, Cu, Sn and S were ground in an agate mortar with a stoichiometric ratio of 2-1-3 to synthesize the $Cu_2SnS_3$ precursor. The ground powders were compacted into a pellet, sealed in an evacuated silica tube and heated to 1023 K at a rate of 50 K min$^{-1}$. The pellet was held at that temperature for 48h followed by a cooling step down to room temperature at a rate of 50 K min$^{-1}$. Subsequently, the as-prepared $Cu_2SnS_3$ was then used as a precursor to produce $Cu_5Sn_2S_7$, $Cu_{5.133}Sn_{1.866}S_7$, $Cu_5Sn_2S_{6.65}Cl_{0.35}$, $Cu_{5.133}Sn_{1.866}S_{6.65}Cl_{0.35}$, and $Cu_{5.133}Sn_{1.866}S_{6.3}Cl_{0.70}$ using Cu, S and CuCl to adjust the stoichiometry. The mixture was ground in an agate mortar, compacted and a second firing was carried out at 873 K for 24h with an intermediate step at 673 K for 12h. The same heating and cooling rates of 50 K min$^{-1}$ were used. The obtained powders were once again ground and sieved down to 200 µm to remove large agglomerates. The powders were then placed in graphite die of 10 mm diameter and densified by SPS (FCT HPD 25) at 873 K for 30 min under a pressure of 64 MPa. The final dimensions of the pellets are around 8 mm in thickness and 10 mm in diameter. Densities were higher than 99 % of the theoretical ones.

### *High-temperature electrical and thermal properties measurements*

The electrical resistivity, $\rho$, and Seebeck coefficient, $S$, were measured simultaneously using an ULVAC-ZEM3 device under partial helium pressure on $3\times3\times10$ mm$^3$ ingots, from 300 K up to 700 K. A NETZSCH LFA-457 apparatus was used for measuring the thermal diffusivity under argon flow. The thermal conductivity, $\kappa$, was determined as the product of the volumetric mass, thermal diffusivity, and theoretical heat capacity estimated using the Dulong−Petit approximation. The lattice contribution to the thermal conductivity, $\kappa_L$, was determined by subtracting the estimated electronic component, $\kappa_e$, from the measured total thermal conductivity, $\kappa$. The electronic contribution, $\kappa_e$, was derived from the Wiedemann-Franz law, $\kappa_e = L\sigma T$, where $L$ is the Lorenz number. The temperature dependence of $L$ was approximated from the Seebeck coefficient using the simplified expression $L = 1.5 + \exp(-|S|/116)$, with |S| expressed in μV K$^{-1}$, from Kim *et al.*[67] The estimated measurement uncertainties are 6% for the Seebeck coefficient, 8% for the electrical resistivity, 11% for the thermal conductivity, and 16% for the dimensionless thermoelectric figure of merit $ZT$.[68]

*Low-temperature electrical and thermal properties measurements*

Hall effect measurements were carried out using Physical Properties Measurement System (PPMS; Quantum Design) under an applied magnetic field up to 9T from 5 K to 300 K, however, some data at the extreme ends of this temperature have been excluded because of the high instrumental errors arising from unstable temperature. Electrical and thermal transport properties between 5 and 300 K were measured continuously using the Thermal Transport Option (TTO) in a Physical Properties Measurement System (PPMS; Quantum Design) with a cooling rate of 0.25 K min$^{-1}$. Specific heat $C_p$ measurements were performed between 1.9 and 300 K by a conventional relaxation method using the dedicated $^4$He option of the PPMS. Small polycrystalline pieces of the monoclinic and cubic phases of approximately 15 mg were glued onto the sample holder by using a minute amount of Apiezon N grease. Details of the equation used to model the low-temperature specific heat data are given in the supporting information.

*X-ray powder diffraction*

X-ray powder diffraction (XRPD) data were collected at room temperature using a Bruker D8 Advance Vario 1 two-circle diffractometer (θ-2θ Bragg-Brentano mode) using Cu Kα radiation ($\lambda$ = 1.5406 Å) with a Ge (111) monochromator (Johansson type) and a Lynx Eye detector. The XRPD data analyses were performed by Rietveld refinement using the FullProf and WinPlotr software packages.[69,70] Background contribution to the XRPD patterns were estimated manually. Zero-point shift, peak shape parameters, asymmetry parameters, lattice parameters, fractional atomic coordinates and isotropic displacement parameters (*i.e.* Debye-Waller factors $B_{iso}$) were finally refined.

*Mössbauer spectroscopy*

$^{119}$Sn Mössbauer spectra of polycrystalline powders with natural abundance of $^{119}$Sn isotope and a real density of ~15 mg cm$^{-2}$ were recorded at 15K in transmission geometry with a spectrometer operated in the conventional constant-acceleration mode. The source, kept at room temperature, was $Ba^{119m}SnO_3$ with a nominal strength of 10 mCi. A palladium foil of 0.5 mm thickness was used as a critical absorber for tin X-rays. Velocity calibration was performed against a 12 mm-thick α-Fe foil at room temperature. $^{119}$Sn isomer shifts (IS) are referred to $BaSnO_3$ at 300 K. Mössbauer spectra were fitted with a least-squares method program assuming Lorentzian peaks.

*EXAFS/XANES*

X-ray absorption spectroscopy (XAS) measurements were carried out at room temperature in transmission mode at the K-edge of Cu (8987.96 eV) and Sn (29 209.79 eV) at the beamline SAMBA (Spectroscopies Applied to Materials Based on Absorption) at Soleil Synchrotron, France (Proposal 20 200 538).[71] Radiation coming from a bending magnet source was collimated by a first cylindrical bent mirror onto the Si(220) fixed exit sagittally-focusing double-crystal monochromator. Harmonic rejection has been performed by the use of a second cylindrical bent mirror that also focused vertically the monochromatic beam.

At the sample position, the spot resulted of 300 × 300 mm$^2$. Measurements have been collected during continuous monochromator scans monitoring, incident, and transmitted X-ray flux by opportunely filled Oxford ionization chambers.[72] During measurement, a reference sample (a copper or a tin foil) has been simultaneously measured with residual photons of the second ionization chamber for energy calibration. The amount of sample and the thickness of the pellet were optimized in order to have proper XAS signal. The calculated amount of each sample was ground, mixed with cellulose, and then compacted into a pellet. Due to the large difference of X-ray cross section at Sn and Cu K edges, two different samples were prepared for the two energies. The Extended X-ray Absorption Fine Structure (EXAFS) signal treatment was performed according to standard procedures: subtraction of the pre-edge and post-edge backgrounds, edge normalization, extraction of EXAFS signal $\chi(k)$ and its Fourier transformation, which provides a map in the real space of the distribution of the distances $R$ around the absorber atom. Demeter software package was used to perform data treatment and fitting.[73] The model functions were created based on the crystallographic data atom location. For each edge, the entire spectrum has been simultaneously fitted, using a single common edge shift. Such approximation has been possible due the strong resemblance of all the spectra and the convention to use exactly the same $E_0$ during the procedure of EXAFS signal extraction.

*Microscopy*

Transmission electron microscopy (TEM) experiment, including electron diffraction (ED), high angle annular dark field scanning TEM (HAADF-STEM) and EDX-STEM studies, was performed on double aberration corrected JEOL ARM200F cold FEG microscope, operated at 200 KV and equipped with CENTURIO large angle EDX detector, ORIUS CCD camera and Quantum GIF. TEM sample was prepared in conventional way by crushing material in agate mortar in ethanol and depositing prepared suspension on Ni holly carbon grid. The short-range ordering model was created using CristaKit software and simulation of ED pattern done using MacTempas program.

*First principles calculations*

All the calculations were done using the quantum ESPRESSO[74] package as embedded in the high-throughput infrastructure AFLOW$\pi$.[75] We used norm-conserving PBE pseudopotentials,[76] well converged basis sets corresponding to an energy cutoff of 150 Ry for the wave functions and 600 Ry for the charge density, and the ACBN0 functional approach[77] have been used to self-consistently determine the values for the Hubbard corrections for each atomic species of the material. To integrate over the Brillouin zone during the self-consistent cycle, a 4 × 4 × 4 and a 4 × 4 × 4 (shifted) grids were used for the 64 atoms and 216 atoms cells respectively. Electronic transport properties like, Seebeck coefficient $S$ and electrical conductivity $\sigma$, were computed by solving Boltzmann transport equation within the constant relaxation time and the rigid band approximation as implemented in PAOFLOW.[78]

We notice that, due to the loss of real periodicity, the Bloch theorem is no longer valid and properties that depend on the crystalline momentum **k** cannot be used. Band structures are not properly representing the electronic structure of a disordered system due to the broken translational invariance. Density of states (DOS) and transport coefficient, however, do not depend explicitly on the crystalline momentum (they are integrated quantities) and, when properly averaged on several representative models, are more realistic.

### *Thermal analysis*

Simultaneous TG and DSC analyses were carried out on cold-pressed pre-SPS powders using a Netzsch DSC 404 F3 Pegasus with a 10 K min$^{-1}$ heating rate.

## ASSOCIATED CONTENT

**Supporting Information**.

Additional figures and tables are available in the supporting information, including XRD patterns and Rietveld refinements, XANES spectra, Hall carrier concentration and mobility, low-temperature transport properties measurements, estimation of the lattice and electronic contributions to the thermal conductivity, theoretical TE performances, electronic band structures and density of states, Electron localization factor (ELF), cycling transport properties measurements, TGA/DSC, calculated formation energies per atom and crystallographic data used for DFT simulations.

AUTHOR INFORMATION

**Corresponding Author**

* emmanuel.guilmeau@ensicaen.fr; marco.fornari@cmich.edu

**Author Contributions**

The manuscript was written through contributions of all authors. All authors have given approval to the final version of the manuscript.

**Funding Sources**

The authors acknowledge the financial support of the French Agence Nationale de la Recherche LabEx EMC3 through the Project FACTO (Grant No. ANR-10-LABX-09-01), the Normandy Region (Réseau d'Intérêt Normand - Label d'excellence), CARNOT ESP and FEDER.

**ACKNOWLEDGMENTS**

The authors gratefully thank Christelle Bilot and Jerôme Lecourt for technical support. The authors acknowledge SOLEIL for provision of synchrotron radiation facilities (proposal 20200538) and we would like to thank Landrot Gautier and Zitolo Andrea for assistance in using beamline Samba. 10.1002/anie.202108686. The authors acknowledge the financial support of the French Agence Nationale de la Recherche LabEx EMC3 through the Project FACTO (Grant No. ANR-10-LABX-09-01), the Normandy Region (Réseau d'Intérêt Normand - Label d'excellence) and FEDER.

REFERENCES

1. Powell, A. V. Recent developments in Earth-abundant copper-sulfide thermoelectric

materials. *J. Appl. Phys.* **126**, 100901 (2019).

2. Shi, X.-L., Zou, J. & Chen, Z.-G. Advanced Thermoelectric Design: From Materials and Structures to Devices. *Chem. Rev.* **120**, 7399–7515 (2020).
3. Dennler, G. *et al.* Are Binary Copper Sulfides/Selenides Really New and Promising Thermoelectric Materials? *Adv. Energy Mater.* **4**, 1301581 (2014).
4. Ge, Z.-H. *et al.* Low-cost, abundant binary sulfides as promising thermoelectric materials. *Mater. Today* **19**, 227–239 (2016).
5. Chen, X. *et al.* Exploring Thermoelectric Property Improvement for Binary Copper Chalcogenides . *Frontiers in Materials* **7**, 373 (2020).
6. Lu, X. *et al.* High performance thermoelectricity in earth-abundant compounds based on natural mineral tetrahedrites. *Adv. Energy Mater.* **3**, 342–348 (2013).
7. Suekuni, K., Tsuruta, K., Ariga, T. & Koyano, M. Thermoelectric properties of mineral tetrahedrites Cu 10Tr 2Sb 4S 13 with low thermal conductivity. *Appl. Phys. Express* **5**, 2–5 (2012).
8. Suekuni, K. *et al.* High-performance thermoelectric mineral Cu12-xNixSb4S13 tetrahedrite. *J. Appl. Phys.* **113**, 043712 (2013).
9. Chetty, R., Bali, A. & Mallik, R. C. Tetrahedrites as thermoelectric materials: An overview. *J. Mater. Chem. C* **3**, 12364–12378 (2015).
10. Barbier, T. *et al.* Structural stability of the synthetic thermoelectric ternary and nickel-substituted tetrahedrite phases. *J. Alloys Compd.* **634**, 253–262 (2015).
11. Barbier, T. *et al.* Thermoelectric Materials: A New Rapid Synthesis Process for Nontoxic and High-Performance Tetrahedrite Compounds. *J. Am. Ceram. Soc.* **99**, 51–56 (2016).
12. Gonçalves, A. P. & Lopes, E. B. Towards the Use of Cu–S Based Synthetic Minerals for Thermoelectric Applications. *Semiconductors* **53**, 1817–1824 (2019).

13. Suekuni, K. *et al.* Retreat from Stress: Rattling in a Planar Coordination. *Adv. Mater.* **30**, 1706230 (2018).

14. Qiu, P., Zhang, T., Qiu, Y., Shi, X. & Chen, L. Sulfide bornite thermoelectric material: A natural mineral with ultralow thermal conductivity. *Energy Environ. Sci.* **7**, 4000–4006 (2014).

15. Guélou, G., Powell, A. V. & Vaqueiro, P. Ball milling as an effective route for the preparation of doped bornite: Synthesis, stability and thermoelectric properties. *J. Mater. Chem. C* **3**, 10624–10629 (2015).

16. Pavan Kumar, V. *et al.* Copper Hyper-Stoichiometry: The Key for the Optimization of Thermoelectric Properties in Stannoidite Cu8+xFe3-xSn2S12. *J. Phys. Chem. C* **121**, 16454–16461 (2017).

17. Pavan Kumar, V. *et al.* Designing a Thermoelectric Copper-Rich Sulfide from a Natural Mineral: Synthetic Germanite Cu22Fe8Ge4S32. *Inorg. Chem.* **56**, 13376–13381 (2017).

18. Pavan Kumar, V. *et al.* Crossover from germanite to renierite-type structures in Cu22-xZnxFe8Ge4S32 thermoelectric sulfides. *ACS Appl. Energy Mater.* **2**, 7679–7689 (2019).

19. Paradis-Fortin, L. *et al.* Structure, microstructure and thermoelectric properties of germanite-type Cu22Fe8Ge4S32 compounds. *J. Alloys Compd.* **831**, 154767 (2020).

20. Liu, M. L., Huang, F. Q., Chen, L. D. & Chen, I. W. A wide-band-gap p -type thermoelectric material based on quaternary chalcogenides of Cu2ZnSnQ4 (Q=S,Se). *Appl. Phys. Lett.* **94**, 202103 (2009).

21. Yang, H., Jauregui, L. A., Zhang, G., Chen, Y. P. & Wu, Y. Nontoxic and abundant copper zinc tin sulfide nanocrystals for potential high-temperature thermoelectric energy harvesting. *Nano Lett.* **12**, 540–545 (2012).

22. Bourgès, C. *et al.* Low thermal conductivity in ternary Cu4Sn7S16 compound. *Acta Mater.* **97**, 180–190 (2015).

23. Cui, J., He, T., Han, Z., Liu, X. & Du, Z. Improved thermoelectric performance of solid solution Cu4Sn7.5S16 through isoelectronic substitution of Se for S. *Sci. Rep.* **8**, 8202 (2018).

24. Tsujii, N., Mori, T. & Isoda, Y. Phase stability and thermoelectric properties of CuFeS2-based magnetic semiconductor. *J. Electron. Mater.* **43**, 2371–2375 (2014).

25. Suekuni, K. *et al.* High-performance thermoelectric minerals: Colusites Cu 26 V 2 M 6 S 32 (M = Ge, Sn). *Appl. Phys. Lett.* **105**, 132107 (2014).

26. Suekuni, K., Kim, F. S. & Takabatake, T. Tunable electronic properties and low thermal conductivity in synthetic colusites Cu26-xZnxV2M6S 32 (x < 4, M = Ge, Sn). *J. Appl. Phys.* **116**, 063706 (2014).

27. Bourgès, C. *et al.* Structural analysis and thermoelectric properties of mechanically alloyed colusites. *J. Mater. Chem. C* **4**, 7455–7463 (2016).

28. Bourgès, C. *et al.* High-Performance Thermoelectric Bulk Colusite by Process Controlled Structural Disordering. *J. Am. Chem. Soc.* **140**, 2186–2195 (2018).

29. Pavan Kumar, V. *et al.* High Power Factors of Thermoelectric Colusites Cu26T2Ge6S32 (T = Cr, Mo, W): Toward Functionalization of the Conductive "Cu–S" Network. *Adv. Energy Mater.* **9**, 1803249 (2019).

30. Guélou, G. *et al.* A scalable synthesis route for multiscale defect engineering in the sustainable thermoelectric quaternary sulfide Cu26V2Sn6S32. *Acta Mater.* **195**, 229–239 (2020).

31. Pavan Kumar, V. *et al.* Copper-rich thermoelectric sulfides: size mismatch effect and chemical disorder in the [TS4]Cu6 complexes of Cu26T2Ge6S32 (T = Cr, Mo, W) colusites. *Angew. Chemie Int. Ed.* **58**, 15455–15463 (2019).

32. Guélou, G., Lemoine, P., Raveau, B. & Guilmeau, E. Recent developments in high-performance thermoelectric sulphides: an overview of the promising synthetic colusites. *J. Mater. Chem. C* **9**, 773–795 (2021).

33. Hagiwara, T. *et al.* Key Role of d0 and d10 Cations for the Design of Semiconducting Colusites: Large Thermoelectric ZT in Cu26Ti2Sb6S32 Compounds. *Chem. Mater.* **33**, 3449–3456 (2021).

34. Deng, T. *et al.* Thermoelectric properties of non-stoichiometric Cu2+xSn1−xS3 compounds. *J. Appl. Phys.* **126**, 85111 (2019).

35. Shen, Y. *et al.* Eco-friendly p-type Cu2SnS3 thermoelectric material: crystal structure and transport properties. *Sci. Rep.* **6**, 32501 (2016).

36. Zhao, H. *et al.* Cobalt-doping in Cu2SnS3: enhanced thermoelectric performance by synergy of phase transition and band structure modification. *J. Mater. Chem. A* **5**, 23267–23275 (2017).

37. Tan, Q., Sun, W., Li, Z. & Li, J.-F. Enhanced thermoelectric properties of earth-abundant Cu2SnS3 via In doping effect. *J. Alloys Compd.* **672**, 558–563 (2016).

38. Zhang, Z. *et al.* Role of crystal transformation on the enhanced thermoelectric performance in Mn-doped Cu2SnS3. *J. Alloys Compd.* **780**, 618–625 (2019).

39. Xu, X. *et al.* Synergistic role of Ni-doping in electrical and phonon transport properties of Cu2Sn1-xNixS3. *J. Alloys Compd.* **728**, 701–708 (2017).

40. Zhao, L. *et al.* Magnetic iron doping in Cu2SnS3 ceramics for enhanced thermoelectric transport properties. *J. Appl. Phys.* **125**, 95107 (2019).

41. Zhou, W. *et al.* Enhancement of the Thermoelectric Figure of Merit in Blended Cu2Sn1–xZnxS3 Nanobulk Materials. *ACS Appl. Nano Mater.* **1**, 4819–4827 (2018).

42. Xi, L. *et al.* Chemical bonding, conductive network, and thermoelectric performance of the ternary semiconductors Cu2SnX3 (X= Se, S) from first principles. *Phys. Rev. B*

**86**, 155201 (2012).

43. Raveau, B. Copper Mixed Valence Concept: “Cu(I)–Cu(II)” in Thermoelectric Copper Sulfides—an Alternative to “Cu(II)–Cu(III)” in Superconducting Cuprates. *J. Supercond. Nov. Magn.* **33**, 259–263 (2019).

44. Zhou, W. *et al.* Sustainable thermoelectric materials fabricated by using Cu2Sn1-xZnxS3 nanoparticles as building blocks. *Appl. Phys. Lett.* **111**, 263105 (2017).

45. Deng, T. *et al.* Discovery of high-performance thermoelectric copper chalcogenide using modified diffusion-couple high-throughput synthesis and automated histogram analysis technique. *Energy Environ. Sci.* **13**, 3041–3053 (2020).

46. Pavan Kumar, V. *et al.* Ordered sphalerite derivative Cu5Sn2S7: a degenerate semiconductor with high carrier mobility in the Cu–Sn–S diagram. *J. Mater. Chem. A* **9**, 10812–10826 (2021).

47. Pavan Kumar, V. *et al.* Local disorder-induced low thermal conductivity in degenerate semiconductor Cu22Sn10S32. *Inorg. Chem.* **60**, 16273 (2021)

48. Deng, T. *et al.* A low-cost and eco-friendly Br-doped Cu7Sn3S10 thermoelectric compound with zT around unity. *J. Mater. Chem. A* **9**, 7946–7954 (2021).

49. Wyckoff, R. W. G. & Posnjak, E. The crystal structures of the cuprous halides. *J. Am. Chem. Soc.* **44**, 30–36 (1922).

50. Lemoine, P., Guélou, G., Raveau, B. & Guilmeau, E. Crystal structure classification of copper-based sulphides as a tool for the design of inorganic functional materials. *Angew. Chemie Int. Ed.*, (2021) DOI: 10.1002/anie.202108686.

51. Lippens, P. E. Interpretation of the 119Sn Mössbauer isomer shifts in complex tin chalcogenides. *Phys. Rev. B* **60**, 4576–4586 (1999).

52. Yamanaka, T. & Kato, A. Moessbauer effect study of 57Fe and 119Sn in stannite, stannoidite, and mawsonite. *Am. Mineral.* **61**, 260–265 (1976).

53. Candolfi, C. *et al.* Disorder-driven glasslike thermal conductivity in colusite Cu26V2Sn6S32 investigated by Mössbauer spectroscopy and inelastic neutron scattering. *Phys. Rev. Mater.* **4**, 25404 (2020).

54. Hegedüs, M. *et al.* Promoted crystallisation and cationic ordering in thermoelectric Cu26V2Sn6S32 colusite by eccentric vibratory ball milling. *Dalt. Trans.* **49**, 15828–15836 (2020).

55. Lippens, P. E., Olivier-Fourcade, J. & Jumas, J. C. Interpretation of the 119Sn Mössbauer parameters. *Hyperfine Interact.* **126**, 137–141 (2000).

56. Wardell, J. L. *Encyclopedia of Inorganic Chemistry*. Chapter Tin: Inorganic Chemistry, Wiley, p. 1-44 (2006).

57. Kumar, P., Nagarajan, R. & Sarangi, R. Quantitative X-ray absorption and emission spectroscopies: electronic structure elucidation of Cu2S and CuS. *J. Mater. Chem. C* **1**, 2448–2454 (2013).

58. Harrison, J. W. & Hauser, J. R. Alloy scattering in ternary III-V compounds. *Phys. Rev. B* **13**, 5347–5350 (1976).

59. Xie, H. *et al.* The intrinsic disorder related alloy scattering in ZrNiSn half-Heusler thermoelectric materials. *Sci. Rep.* **4**, 6888 (2014).

60. Ibrahim, D. *et al.* Comprehensive study of the low-temperature transport properties of polycrystalline $Sn_{1+x}Te$ (x=0 and 0.03). *Phys. Rev. Mater.* **3**, 85404 (2019).

61. Guélou, G. *et al.* Toppling the Transport Properties with Cationic Overstoichiometry in Thermoelectric Colusite: [Cu26Cr2Ge6]1+δS32. *ACS Appl. Energy Mater.* **3**, 4180–4185 (2020).

62. McKinney, R. W., Gorai, P., Stevanović, V. & Toberer, E. S. Search for new thermoelectric materials with low Lorenz number. *J. Mater. Chem. A* **5**, 17302–17311 (2017).

63. Thesberg, M., Kosina, H. & Neophytou, N. On the Lorenz number of multiband materials. *Phys. Rev. B* **95**, 125206 (2017).

64. Prokof'eva, L. V., Shabaldin, A. A., Korchagin, V. A., Nemov, S. A. & Ravich, Y. I. Lorentz number and Hall factor in degenerate semiconductors during resonance scattering of charge carriers. *Semiconductors* **42**, 1161 (2008).

65. Misra, S. *et al.* Band structure engineering in $Sn_{1.03}Te$ through an In-induced resonant level. *J. Mater. Chem. C* **8**, 977–988 (2020).

66. Lemoine, P. *et al.* High temperature neutron powder diffraction study of the Cu12Sb4S13 and Cu4Sn7S16 phases. *J. Solid State Chem.* **247**, 83–89 (2017).

67. Kim, H.-S. S., Gibbs, Z. M., Tang, Y., Wang, H. & Snyder, G. J. Characterization of Lorenz number with Seebeck coefficient measurement. *APL Mater.* **3**, 1–6 (2015).

68. Alleno, E. *et al.* Invited Article: A round robin test of the uncertainty on the measurement of the thermoelectric dimensionless figure of merit of Co0.97Ni0.03Sb3. *Rev. Sci. Instrum.* **86**, 11301 (2015).

69. Rodríguez-Carvajal, J. Recent advances in magnetic structure determination by neutron powder diffraction. *Phys. B Condens. Matter* **192**, 55–69 (1993).

70. Roisnel, T. & Rodríquez-Carvajal, J. WinPLOTR: A Windows Tool for Powder Diffraction Pattern Analysis. *Mater. Sci. Forum* **378**–**381**, 118–123 (2001).

71. Briois, V. *et al.* SAMBA: The 4–40 keV X-ray absorption spectroscopy beamline at SOLEIL. *UVX 2010 - 10e Colloq. sur les Sources Cohérentes Incohérentes UV, VUV X ; Appl. Développements Récents* 41–47 (2011).

72. Pettifer, R. F., Borowski, M. & Loeffen, P. W. The physics of ionization chambers - or how to improve your signal-to-noise ratio for transmission EXAFS measurements. *J. Synchrotron Radiat.* **6**, 217–219 (1999).

73. Ravel, B. & Newville, M. ATHENA, ARTEMIS, HEPHAESTUS: data analysis for X-

ray absorption spectroscopy using IFEFFIT. *J. Synchrotron Radiat.* **12**, 537–541 (2005).

74. Giannozzi, P. *et al.* QUANTUM ESPRESSO: a modular and open-source software project for quantum simulations of materials. *J. Phys. Condens. Matter* **21**, 395502 (2009).

75. Supka, A. R. *et al.* AFLOWπ: A minimalist approach to high-throughput ab initio calculations including the generation of tight-binding hamiltonians. *Comput. Mater. Sci.* **136**, 76–84 (2017).

76. Hamann, D. R. Optimized norm-conserving Vanderbilt pseudopotentials. *Phys. Rev. B* **88**, 85117 (2013).

77. Agapito, L. A., Curtarolo, S. & Buongiorno Nardelli, M. Reformulation of $\mathrm{DFT}+U$ as a Pseudohybrid Hubbard Density Functional for Accelerated Materials Discovery. *Phys. Rev. X* **5**, 11006 (2015).

78. Buongiorno Nardelli, M. *et al.* PAOFLOW: A utility to construct and operate on ab initio Hamiltonians from the projections of electronic wavefunctions on atomic orbital bases, including characterization of topological materials. *Comput. Mater. Sci.* **143**, 462–472 (2018).

## Table of Content